PCCP

Accepted Manuscript

ROYAL SOCIETY OF CHEMISTRY

www.rsc.org/pccp

Journal Name

ARTICLE

Rose Bengal incorporated in mesostructured silica nanoparticles: structural characterization, theoretical modeling and singlet oxygen delivery

Received 00th January 2015,
Accepted 00th January 2015

DOI: 10.1039/x0xx00000x

www.rsc.org/

B. Martins Estevão[a,b]; F. Cucinotta[a,c]; N. Hioka[b]; M. Cossi[a], M. Argeri[a], G. Paul[a], L. Marchese[a]; E. Gianotti[a*].

Rose Bengal (RB), a xanthene dye, incorporated into mesostructured silica nanoparticles (MSNs) exhibits efficient singlet oxygen ($^1O_2$) generation when illuminated with 540 nm green light which is particularly promising for PDT applications. Several systems with different RB loadings were synthesized and fully characterized by means of spectroscopic techniques in combination with a computational study, to optimize the amount of RB in order to avoid the formation of aggregates that is detrimental for a high $^1O_2$ delivery.

1. Introduction

In the last decade, the functionalization of mesoporous silica nanoparticles with highly fluorescent organic molecules has been intensively addressed to the design of efficient nanoplatforms for bio-medical applications. In particular, the coupling of photosensitizing molecules (PS) to silica nanoparticles has shown attractive perspectives of performing both fluorescence imaging and photodynamic therapy (PDT) of cancer.[1-4] Among the high variety of organic molecules that can be used as PS, halogen-xanthene dyes, such as rose bengal (RB), show intense absorption bands in the green region of the visible spectrum (480-550 nm) and high yield in the generation of singlet oxygen. In particular, rose bengal (4,5,6,7-tetrachloro-2',4',5',7'-tetraiodo-fluorescein disodium, scheme 1) type-II photosensitizer is notable for its high triplet quantum yield (Φ_T = 0.76), fairly long lived triplet state ($t_{1/2}$= 0.1-0.3 ms), and high singlet oxygen quantum yield (Φ $^1O_2$ = 0.75 under 540 nm light irradiation).[5-8] These photophysical properties are very appealing for the use of rose bengal in PDT. In addition, the minimally penetrating nature of the green light makes rose bengal particularly useful in many skin diseases like psoriasis and atopic dermatitis,[9] inhibition of oral cancer DNA polymerases[10] and inactivation of various biological species such as vaccinia virus or Escherichia coli.[11,12] The photodynamic therapy is a minimally-invasive treatment for cancer disease that involves the local administration of PS suitably illuminated by light with a wavelength compatible to PS absorption spectra. The irradiation promotes the PS to its singlet excited state (^{1}PS*), which can undergo to triplet state (^{3}PS*) by a intersystem crossing (ISC) process. The ^{3}PS* can, therefore, interact directly with molecular oxygen to generate singlet oxygen $^1O_2$ (type II mechanism), a highly reactive specie that can produce necrosis and/or apoptosis of diseased tissues and further healing of local injury. Compared to traditional oncological treatments (chemotherapy or radiotherapy), the oxidative damage of PDT is limited to the immediate area surrounding the excited PS, reducing in this way the toxic side effects and the damage on healthy cells.[13-15] Besides photophysical requirements, there are some needs regarding the general properties of PS that must be dealt in order to allow practical applications as low dark toxicity, non-longstanding photosensitivity on epidermis, and ability to avoid mutagenesis along with simple, reproducible and stable formulation, favourable pharmacokinetics, easy administration, and low cost.[16,17] Rose bengal meets most of the requirements as effective candidates for PDT, nevertheless it suffers from poor intracellular uptake ability and thus cannot be used to treat solid tumors.[18] Recent literature reports have demonstrated the use of nanoparticles as the

[a] Department of Science and Technological Innovation and Nano-SiSTeMI Centre, Università del Piemonte Orientale, Viale T. Michel 11, 15121 Alessandria, Italy.
[b] Nucleos Research of Photodynamic Therapy, Chemistry Department, State University of Maringá, Av. Colombo 5.790, 87020-900, Maringá, Paraná, Brazil.
[c] School of Chemistry, Newcastle University, Newcastle upon Tyne, NE1 7RU, United Kingdom.

† Footnotes relating to the title and/or authors should appear here.
Electronic Supplementary Information (ESI) available: [Table S1 reports the weight loss (%) due to the organic content calculated from TGA analysis between 150-900°C after the removal of physisorbed water. Table S2 reports the particle size dimension obtained by DLS. Figure S1 presents the TGA curves of calcined MSNs (curve a), NH-MSNs (curve b), RB-MSNs 1% (curve c), 4% (curve d) and 10% (curve e). In Figure S2, UV-Vis spectra of RB-MSNs 1% eluates after washing the RB-MSNs 1% solid samples prepared by physical adsorption of RB (curve a) and by covalent bond of RB (curve b) to the MSNs nanoparticles are reported. In Figure S3, the N_2 adsorption-desorption isotherms at 77K of NH_2-MSNs, RB-MSNs 1%, 4% and 10% are reported. Figure S4 reports the UV-Vis spectra of RB-MSNs and RB in water solution upon irradiation with visible light for several days. Figure S5 represents the orbitals involved in the visible and UV main peak transitions and Figure S6 represent the orbitals involved in the triplet state. In Figure S7, the absorption spectra of UA in the presence of RB and RB-MSNs 1%; 4% and 10% in water after different irradiation times with 540 nm light are reported]. See
DOI: 10.1039/x0xx00000x

vehicle to conjugate with PS in order to enhance the uptake efficiency by cancer cells without affecting the photodynamic properties of the PS.[19] However, many currently developed PS molecules are hydrophobic and tend to aggregate easily in aqueous media, leading to a decrease in their quantum yields and problems for intravenous administration.[20] The use of nanoparticles to carry the PS has thus been widely explored, aiming at solving all or some of the problems in traditional PDT using free PS agents. In fact, the large surface to volume ratio of the nanoparticles would enable them to carry optimum PS concentration to the target cells, and unique properties like size/shape tuneable nature, simple surface modification and stability provide nanoparticles advantageous over pure molecular therapeutics.[21] To date, various types of nanodevices, such as polymeric micelles, liposomes, metal oxides, quantum dots, mesoporous silica and gold nanoparticles, have been used as platforms to integrate therapeutic and diagnostic functions in a single nanoparticle.[22] Ordered mesoporous silica nanoparticles (MSNs) have recently garnered considerable attention in nano-medicine as potential theranostic platforms largely due to their tunable size and pore diameter, high pore volume (0.6–1.0 ml/g) excellent biocompatibility, intrinsically large surface area (600–1000 m^2/g), and topologically distinct domains that can be individually functionalized. Moreover, the porous silica structure does not only act as a suitable carrier for hydrophobic molecules but may also protect the loaded molecules from degradation. Finally, the surface chemistry of the MSNs can be fine-tuned for a specific biological application, for example in order to optimize the interaction between a drug molecule of interest and the silica support, for optimizing dispersion stability and/or cellular uptake, for covalent attachment of imaging agents and targeting ligands to the particles, and for rational control of drug release rate.[2,3] Herein, amino-functionalized MSNs were synthesized to conjugate rose bengal (RB) through covalent bonding to yield RB-modified MSNs (RB-MSNs) for PDT study. To optimize the PS concentration and dispersion coupled with a high efficiency of $^1O_2$ release, several nanosystems with different RB loadings were synthesized. The high surface area of the MSNs allows to host high concentration of guest molecules, nevertheless not always a high cargo of molecules inside the mesopores corresponds to a better efficiency of singlet oxygen generation. In fact, aggregation is important in PDT because it occurs readily between PS molecules in water-rich media and the photophysical properties of aggregate species are different from those of the monomer. In particular, the aggregate is usually found to have lower $^1O_2$ quantum yield and therefore a lower photodynamic efficacy induced by non-fluorescent dimers. By covalently coupling the PS into a nanoparticle, it is thus possible to reduce aggregation.

A detailed structural and morphological characterization of the RB-MSNs was performed by X-ray powder diffraction (XRD), high-resolution transmission electron microscopy (HRTEM) and volumetric and thermogravimetric analysis combined with FTIR and SS-NMR techniques, extending the partial characterization of the RB-MSNs 4% reported in ref.23. To elucidate the RB distribution within the pores of MSNs with respect to the RB loadings and the influence of the encapsulation on the photoemission properties of the guests, a detailed spectroscopic characterization was carried out by using Diffuse Reflectance (DR) UV-Vis and photoluminescence. Due to the potential application of such nanosystems for PDT, the $^1O_2$ generation efficiency was evaluated by a chemical method using uric acid, which undergoes oxidation upon the RB irradiation and $^1O_2$ generation. The structure of RB in water solution and immobilized into the channel of MSNs was also optimized theoretically, with Density Functional Theory (DFT) methods, to understand the structural modifications induced by the adsorption on the silica particles. The UV-Vis spectra were simulated at the Time Dependent DFT level, to support the interpretation of the experimental spectra and again to study the changes due to the adsorption on MSNs. The RB-MSNs with the optimum RB loading has shown interesting performances in the decreasing of melanoma cell proliferation under illumination highlighting the scientific interest and the potential application of such nanosystem as PDT device in nanomedicine.[23]

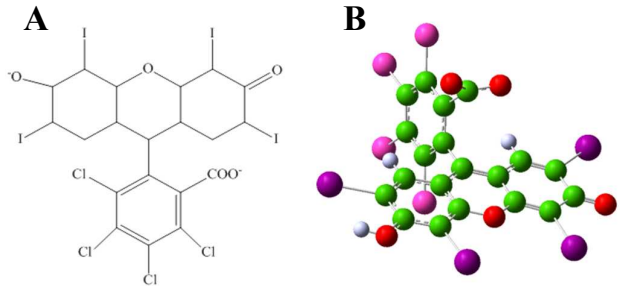

Scheme 1 – Lewis scheme (A) and molecular structure (B) of dianionic Rose Bengal. C: green; H: white, O: red, Cl: light purple; I: purple.

2. Materials and methods

2.1 Synthesis of amino functionalized ordered mesoporous silica nanoparticles: Amino functionalized ordered mesoporous silica nanoparticles (NH_2-MSNs) were prepared according to literature procedures using cetyltrimethylammoniumbromide (CTAB) as a structure directing agent. CTAB (1.9 mmol) was first dissolved in 340 mL of water. Then an aqueous NaOH (2.0 M, 2.45 mL) was added to the CTAB solution, followed by adjusting the solution temperature to 80°C. Finally, tetraethoxy silane (TEOS, 3.5 mL, 18.1 mmol) and 3-aminopropyl triethoxy silane (APTES, 0.43 mL, 2.04 mmol) were added simultaneously dropwise to the solution for a period of 4 minutes. The mixture was stirred at 80°C for 2 hours to give rise to white precipitates (as synthesized NH_2-MSNs). The solid product was filtered, washed with deionized water and ethanol, and dried in vacuo.[24] The surfactant template (CTAB) was removed by Soxhlet extraction with 2-propanol/HCl for 96 hours at 200°C.

2.2 Covalent conjugation of Rose Bengal with NH_2-MSNs:

Extracted NH_2-MSNs were firstly dispersed in 15 mL of DMF (N,N-dimethylformamide) and then sonicated for 15 minutes. To covalently conjugate RB to NH_2-MSNs, a DMF solution (15mL) containing Rose Bengal (RB, 1 eq.), 1-[Bis(dimethylamino)methylene]-1H-1,2,3-triazolo[4,5-b]pyridinium 3-oxid hexafluorophosphate (HATU, 1 eq.) and N,N-diisopropylethylamine (DIPEA, 2 eq.) was added to the NH_2-MSNs dispersion and stirred vigorously for 24 h at room temperature and protected from light. The solid hybrid was then filtered and dried under vacuum.[23] Three RB containing NH_2-MSNs materials (labelled RB-MSNs) were prepared with an increase RB loading in the range of 10 to 100 mg/g. The as-synthesized RB-MSNs solids were washed several times with DMF to remove the un-reacted RB molecules. The actual RB loading (Table 1) was calculated from the RB eluate UV-Vis spectra after the washing procedure using the Lambert-Beer law (ε_{566} = 95780 M^{-1} cm^{-1} in DMF measured from the slope of a plot).

2.3 Characterization methodologies: X-Ray diffraction (XRD) patterns were obtained using an ARL XTRA48 diffractometer with Cu Kα radiation (λ = 1.54062 Å).

HRTEM images were collected on a JEOL 3010 High Resolution Transmission Electron Microscope operating at 300 kV. Specimens were prepared by dispersing the sample by sonication in isopropanol and by depositing a few drops of the suspension on carbon-coated grids.

A dynamic light scattering (DLS) and zeta potential experiment was performed at 37°C on aqueous nanoparticle dispersion sample using Malvern Zetasizer Nano-ZS, Malvern Instrument UK, which uses a 4mW He-Ne laser operating at 633 nm and a detection angle of 173°. Suspensions of 11 μg mL^{-1} and 660 μg mL^{-1} respectively, of each material in buffer solutions (pH = 7.0) were prepared and measured immediately after ultrasonication for 15 min.

Thermogravimetric analyses (TGA/DTG) of materials were performed under argon flow (100 ml min^{-1}) with a SETSYS Evolution TGA-DTA/DSC thermobalance, heating from 40 to 1000 ^{o}C at 5 ^{o}C min^{-1}.

All solid state NMR (SS-NMR) spectra were acquired on a Bruker Avance III 500 spectrometer and a wide bore 11.7 Tesla magnet with operational frequencies for ^{1}H, ^{29}Si and ^{13}C of 500.13, 99.35 and 125.77 MHz, respectively. A 4mm triple resonance probe with Magic Angle Spinning (MAS) was employed in all the experiments. The samples were packed on a Zirconia rotor and spun at a MAS rate between 0 and 15 kHz. The magnitudes of radio frequency fields, υ_{rf}, were 100 and 42 kHz for ^{1}H and ^{29}Si, respectively. The relaxation delays, d1, between accumulations were between 2.5 and 180 s for ^{1}H and ^{29}Si MAS NMR, respectively. For the $^{13}C\{^{1}H\}$ CPMAS experiments, the radio frequency fields υ_{rf}^{H} of 55 and 28 kHz were used for initial excitation and decoupling, respectively. During the CP period the ^{1}H RF field υ_{rf}^{H} was ramped using 100 increments, whereas the ^{13}C RF field υ_{rf}^{C} was maintained at a constant level. During the acquisition, the protons are decoupled from the carbons by using a Two-pulse Phase Modulation (TPPM) decoupling scheme. A moderate ramped RF field υ_{rf}^{H} of 62 kHz was used for spin locking, while the carbon RF field υ_{rf}^{C} was matched to obtain optimal signal and the CP contact time of 2 ms was used. All chemical shifts are reported using δ scale and are externally referenced to TMS at 0 ppm.

FTIR spectra of self-supporting pellets were collected under vacuum conditions (residual pressure $<10^{-5}$ Torr) using a Bruker Equinox 55 spectrometer equipped with a pyroelectric detector (DTGS type) with a resolution of 4 cm^{-1}.

N_2 physisorption measurements were carried out at 77K in the relative pressure range from 1 x 10^{-6} to 1 P/P_0 by using a Quantachrome Autosorb1MP/TCD instrument. Prior to the analysis, the samples were outgassed at 373 K for 3 h (residual pressure lower than 10^{-6} Torr). Specific surface areas were determined using the Brunauer–Emmett–Teller equation, in the relative pressure range from 0.01 to 0.1 P/P_0. The desorption branch of the N_2 physisorption isotherm was analyzed by means of the NLDFT (non local density functional theory) method, to obtain the pore size distribution of the material.[25]

Diffuse Reflectance UV-Vis (DR UV-Vis) spectra were recorded using a Perkin Elmer Lambda 900 spectrometer equipped with a diffuse reflectance sphere attachment.

Photoemission steady state spectra were acquired with a Horiba Jobin Yvon Fluorolog spectrofluorimeter equipped with a 450 W Xenon lamp and a Hamamatsu R928 photomultiplier.

2.4 Indirect Determination of Singlet Oxygen: Uric acid (UA, Sigma Aldrich, 1.0x10^{-4} mol L^{-1}) was used to determine the singlet oxygen generation.[26,27]

The experiments were carried out by irradiating samples with a light source of 540 nm (450 W Xenon lamp) and, after certain time intervals, absorption spectra were collected with a Perkin Elmer Lambda 900 spectrometer. The $^{1}O_2$ scavenger absorption was monitored through a decrease in the electronic absorption band of uric acid around 292 nm. The UA absorption intensity was plotted against irradiation time and the time for UA absorption decrease was calculated by fitting the curve with a bi-exponential decay in the case of RB in water solution[26,27] and with a mono-exponential decay in the case of RB-MSNs nanoparticles. The time for the decrease of the UA absorption (t) is inversely proportional to its reaction rate with singlet oxygen; in the case of RB in water solution the K_1 was used to calculate the time. The measure of singlet oxygen delivery efficiency ($\eta_{(RB\text{-}MSNs)}$) was made adopting the Equation 1 proposed by Rossi et al.:[28]

$$\eta_{(RB-MSNs)} = \Phi_{RB}{}^{1}O_2 \frac{t_{RB}}{t_{(RB-MSNs)}} \quad (1)$$

where t_{RB} is the time for the decrease in absorption of uric acid in the presence of RB in a water solution and $t_{(RB\text{-}MSNs)}$ is the time for the decrease in absorption of UA in the presence of RB-MSNs in a water suspension, and Φ_{RB} is the singlet oxygen quantum yield of RB in a water solution (Φ_{RB} = 0.75).

2.5 Theoretical calculations: all the calculations were performed at the DFT level, with different functionals and

basis sets. Free and adsorbed RB structure optimizations were obtained with B3LYP density functional[29] and 6-311G(d,p) Pople's basis set[30,31] for light atoms, while Hay and Wadt Lanl2dz effective core potentials[32-34] and basis set were used for Cl and I. Solvent (water) effects were reproduced through the Conductor-like Polarizable Continuum Model (CPCM)[35] as implemented in Gaussian09 package. Dispersion energy corrections were included in all the structure calculations with the semiempirical approach proposed by S. Grimme and implemented in Gaussian09 (GD3 procedure).

The absorption spectra were simulated with Time-Dependent (TD)-DFT techniques. Theoretical spectra for free RB in water were computed with a number of pure and hybrid density functionals and basis sets, and compared to the experimental spectrum in the same conditions: the best agreement was obtained with PBE functional[36] and 6-311++G(d,p) basis set, and the same level was kept for simulating the spectra of RB adsorbed on MSN too.

3. Results and discussion

3.1. Synthesis of RB-MSNs nanoparticles

Initially, amine-functionalized MSNs (NH_2-MSNs) were synthesized by a one-pot template route. The amine groups are necessary to conjugate the activated RB. The photosensitizer RB was covalently attached to the amino groups of NH_2-MSNs nanoparticles as reported in Scheme 2 and three RB-MSNs samples with different RB loadings were synthesized.

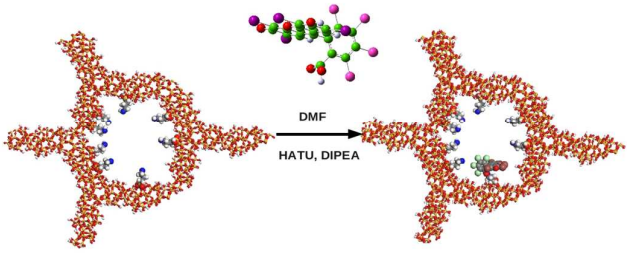

Scheme 2 - Schematic representation of the synthetic procedure used to obtain RB-MSNs nanoparticles.

To evaluate the actual RB loadings (Table 1), all the samples were washed several times with water to remove the un-reacted RB molecules and eluates were analyzed by UV-Vis absorption spectroscopy.

Table 1 - RB loadings used during the RB-MSNs synthesis (Nominal RB) and after washing procedures (Actual RB) together with the average number of RB molecules per NPs and the weight loss % due to RB.

Samples	Nominal RB loading (mg/g)	Actual RB loading (mg/g)	Actual RB loading (μmol/mg)	Efficiency of RB functionalization (%)	Average number of RB molecules per NPs	Δwt% due to RB calculated by TGA
RB-MSNs 1%	10	9.5	0.0097	95	1.1 10^4	1.1
RB-MSNs 4%	40	34.4	0.035	86	4.2 10^4	4.08
RB-MSNs 10%	100	69.2	0.071	69.2	8.5 10^4	7.56

The average number of RB molecules per nanoparticles was also calculated by considering the density of the mesoporous silica nanoparticles[37] and the particle size (Table 1, see Fig.2 and Table S2 in the Supporting Information for the particle size dimension). In Table 1 is also reported the weight loss due to RB molecules calculated by the TGA analysis for all the samples (see the TGA curves in Fig. S1 and Table S1 of the Supporting Information) that is in agreement with the values of RB loading calculated by UV-Vis spectroscopy. RB was also physically adsorbed into the NH_2-MSNs nanoparticles for comparison. In this latter case, after washing the sample almost 60% of RB is washed away (see Fig. S2 in the Supporting Information).

3.2. Characterization of the RB-MSNs nanoparticles

All the RB containing NH_2-MSNs were characterized by XRD, HRTEM, DLS analyses to elucidate structural modification and particle dimensions of the mesoporous nanoparticles after the post-synthetic procedures used to introduce the RB molecules inside the mesopores. In Figure 1, the XRD patterns of plain MSNs and NH_2-MSNs, after template (CTAB) removal, and those of RB-MSNs with different RB loadings are reported. All the materials show the typical XRD pattern of an ordered hexagonal network of mesopores typical of MCM-41 material with (100), (110), (200) and (210) reflections (the last being only partially resolved),[38] indicating that synthetic procedures followed to introduce RB inside the pores of the ordered silica did not affect the structural integrity of MSNs.

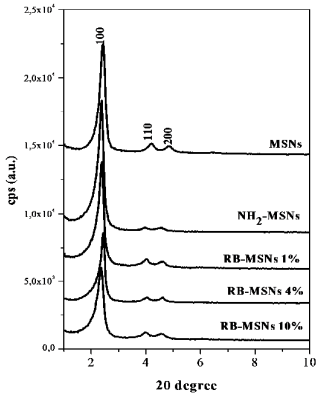

Fig. 1 - XRD patterns of RB-MSNs with different RB loading. The XRD patterns of plain MSNs nanoparticles and NH_2-MSNs, after CTAB removal, were also reported for comparison.

The HRTEM analysis has evidenced that well-ordered nanostructured mesoporous particles are formed and that the average particle size is in the 150-180 nm range (Figure 2), also confirmed by DLS analysis (Table S2 in the Supporting Information).

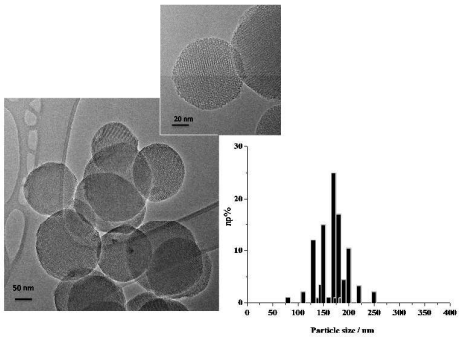

Fig. 2 – HRTEM images of RB-MSNs and particle size distribution.

To confirm that Rose Bengal is still intact after all the synthetic steps necessary to produce RB-MSNs nanoparticles, ^{13}C CP MAS NMR was used (Figure 3). Specifically, the ^{13}C CP/MAS NMR spectrum of the RB-MSNs 10% (curve a) presents the typical signals of RB (curve b) confirming the integrity of the PS after the synthesis process. In fact, in the range between 160–110 ppm, weak signals, due to aromatic carbons, are present, while the peaks due to C-Cl and C-I groups are visible at 126 and 71 ppm respectively. In addition, the peak assigned to C=O groups (165 ppm) and the signal due to C-NH (43 ppm), are also present. At 28 ppm is also present a peak belonging to a residual fraction of DMF solvent. Signals at 22 and 8 ppm are due to CH_2-CH_2-Si of the APTS precursor and signals at 15 and 60 ppm are assignable to unreacted ethoxy groups. ^{29}Si MAS NMR spectrum confirms that the APTS is incorporated covalently into the ordered porous network bound to inorganic silica units. In fact, the ^{29}Si MAS NMR spectrum exhibits band at -65 ppm assigned to T^3-type silicon species having a Si–C covalent bond. In addition, peaks at -100 and -110 ppm are also present, attributed to Q^3 ($Si(OH)(OSi)_3$) and Q^4 ($Si(OSi)_4$) silicon units, respectively, which are typical of highly siliceous conventional mesoporous materials, associated with tetrahedrally coordinated silicon atoms forming the solid network.[39,40]

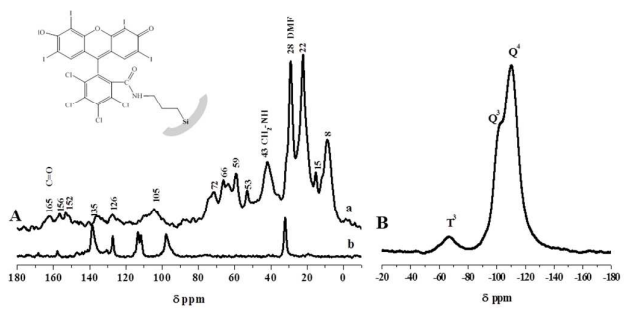

Fig. 3 – ^{13}C MAS NMR (A) of RB-MSNs 10% (curve a) and RB (curve b) and ^{29}Si MAS NMR (B) of RB-MSNs 10% nanoparticles.

The covalent coupling between RB and NH_2-MSNs was confirmed by FTIR spectroscopy (Figure 4), by the presence of the band at 1385 cm^{-1} due to the C-N stretching mode of amide II[41] and by the bands at 1660 and 1600 cm^{-1} due to the C=O stretching and N-H bending modes respectively. The higher intensity of the band at 1660 cm^{-1} in the RB-MSNs 10% sample is due to the high RB loading. The bands in the 1500-1400 cm^{-1} range are due to the bending modes of $–CH_2$ groups.

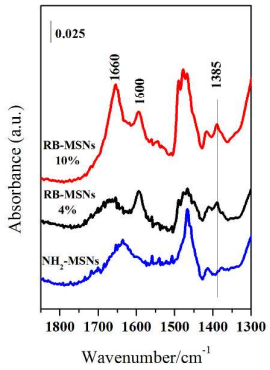

Fig. 4 – FTIR spectra of RB-MSNs (4% and 10%) and NH_2-MSNs.

The textural properties of NH_2-MSNs and RB-loaded MSNs were obtained by N_2 adsorption-desorption isotherms (Fig. S3 in the Supporting Information) at 77K and are reported in Table 3. The functionalized MSNs show type IV isotherms with H1-type hysteresis, which is typical of standard M41S materials. The specific surface area (SSA), pore diameter and pore volume decreased when RB was covalently bound to MSNs and this reduction is more evident with higher RB loadings. This behaviour confirms that RB molecules have been introduced into the mesoporous channels of the silica nanoparticles.

Table 3. Textural properties of RB-MSNs with different RB loadings.

Samples	SSA_{BET} (m^2/g)	D_{DFT} (Å)	V (cm^3/g)
NH_2-MSNs	1150	38	1.38
RB-MSNs 1%	1099	37.5	1.3
RB-MSNs 4%	885	36	0.9
RB-MSNs 10%	749	35	0.7

The structure of RB-MSNs was also optimized at the DFT level: the silica wall was modeled by a finite cluster mimicking MCM-41 internal pore, based on the same model discussed e.g. in ref. 42. The adduct is shown in Figure 5: the RB structure is quite distorted upon adsorption, mainly due to dispersion interactions (simulated by semiempirical Grimme's procedure) which tend to stick the molecule to the silica surface. As a consequence the xanthene moiety is slightly twisted, and xanthene and benzene molecular planes are no longer perpendicular as in the free RB (see Scheme 1).

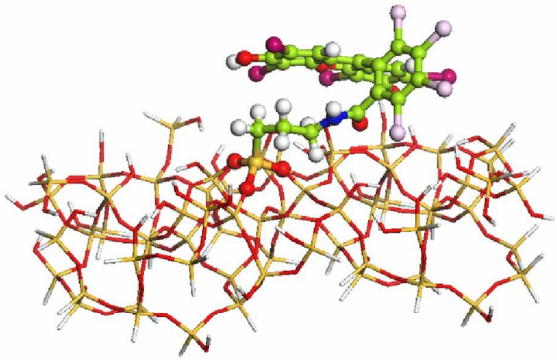

Fig. 5 - Optimized structure of RB attached to the mesoporous silica model.

To elucidate RB dispersion within the channels of MSNs, the UV-Vis features of the RB-MSNs nanoparticles have been investigated by comparison with pure RB in water solution (Figure 6). RB in water solution was studied at a concentration of 10^{-6} M, where RB is present in monomeric form.[43,44] At neutral pH, the absorption maximum of RB in solution is present at 547 nm with a shoulder at 510 nm and it is red-shifted at 564 nm when RB is conjugated to MSNs. This bathochromic shift is ascribed to the confinement effect and to a change of the chemical environment of RB molecules inside the mesoporous channels. In the solid samples (RB-MSNs), the intensity of the visible band (564 nm) increases with the RB loading from 1% to 4% and decreases when the RB loading is 10%, this effect may be due to the formation of RB aggregates.[5,45] Moreover, in the UV range, a broad absorption centered at 245 nm with a prominent shoulder at higher wavelength is present and increases with the RB loading in the case of solid samples, while in the case of RB in water solution a single band at 264 nm is visible.

The protection effect of the inorganic mesoporous structure towards RB photodegradation has been evaluated by the UV-Vis spectra of RB in solution and RB-MSNs 4% and 10% samples upon irradiation with visible light for several days (Fig. S4 in the Supplementary Information). The photobleaching is almost stopped when RB is introduced into MSNs nanoparticles, while is rapid when RB molecules are in solution.

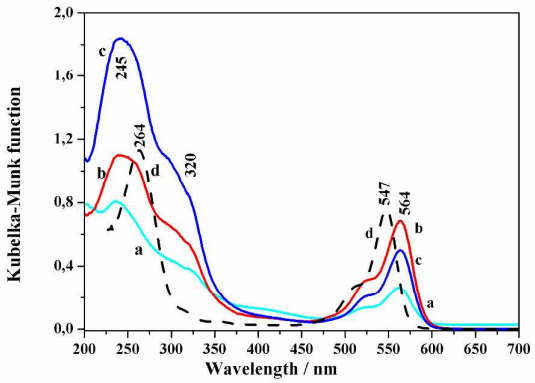

Fig. 6 – DR UV-Vis spectra of RB-MSNs 1% (curve a), RB-MSNs 4% (curve b), RB-MSNs 10% (curve c) and UV-Vis absorption spectrum of RB in water solution (curve d, dotted line).

The absorption spectra of RB in aqueous solution and on MSNs surface were simulated at the TD-DFT level: as explained above, the spectra in water were computed with different functionals and basis sets, reaching the best agreement with PBE/6-311++G(d,p) calculations, as shown in Figure 7A. TD-DFT calculations on the whole RB-MCM adduct are not feasible, due to their excessive computational burden: however, the effect of the molecular distortion can be evaluated by computing the RB absorption spectrum in the deformed geometry extracted from the adduct optimized structure. The result is reported in Figure 7B.

The dye deformation induced by the silica surface causes an upshift of the first absorption band (its wavelength increasing from 535 to 559 nm), and a downshift of the main UV peak (from 290 to 260 nm): this agrees qualitatively with the experiments, where the observed shift are about +17 and -19 nm respectively. Overall, the computed spectrum for the distorted RB molecule is in quite good agreement with the experimental spectrum for the dye adsorbed on MSNs. This allows us to assign the main peaks to particular orbital transitions: the absorption at 559 nm (564 nm in the experimental spectrum) is almost entirely due to the HOMO-LUMO transition, while the main UV peak (260 nm in the simulation, 245 nm experimentally) results from different transitions, involving HOMO-1, HOMO-5, HOMO-13 and LUMO+10 and LUMO+11 orbitals (all the cited orbitals are depicted in Fig. S5 in the Supplementary Information).

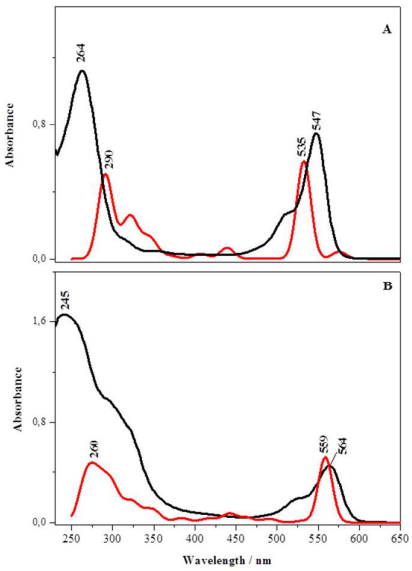

Fig. 7 - A: Simulated (red curve) and experimental (black curve) UV-Vis absorption spectrum of RB dianion in aqueous solution. B: Simulated (red curve) and experimental (black curve) DR UV-Vis spectrum of RB attached to the silica surface. The theoretical spectrum has been computed on the isolated dye, keeping the distorted geometry found for the RB-mesoporous silica adduct.

Excitation and emission spectra of the RB-MSNs with different RB loadings are reported in Figure 8 along with the excitation and emission spectra of the corresponding RB in water solution (inset) for the sake of comparison. The typical excitation spectrum of RB molecules in water solution is characterized by a main contribution at ca. 544 nm, with a higher-energy shoulder at ca. 510 nm, whereas the photoemission spectrum is almost the mirror image, with maximum at ca. 563 nm and a lower-energy shoulder at ca. 611 nm.[44] When RB is conjugated to the MSNs, a red shift of the emission bands is visible (main band at 588 nm and shoulder at 627 nm) and the emission intensity increases along with the increasing loading from 1 to 4%, whereas in the case of the higher loading sample (10%), the emission intensity is the lowest suggesting that a concentration-induced quenching occurs within the channels of silica nanoparticles due to the formation of aggregated species. The relative intensity of the peak to the shoulder is usually used as a measure of the RB aggregation; larger ratio value indicates lesser aggregation.[46] The ratio of the intensities (I_1/I_2) of the peak (λ_1) to the shoulder (λ_2) are reported in Table 4; the RB in water solution is recorded at the concentration of 10^{-6} M, where RB is present predominantly in monomeric form and in fact, the higher value of the ratio is obtained. When RB is introduced in the mesopores of MSNs, the ratio decreased suggesting an incipient formation of RB aggregates that are particular evident in the case of RB-MSNs 10% sample. Nevertheless, the RB-MSNs 1% sample shows the higher value of I_1/I_2 ratio confirming that using low RB loading the formation of dimers are limited.

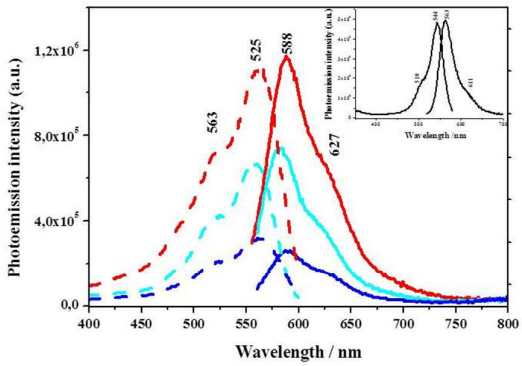

Fig. 8 – Steady state excitation (λ_{em}= 620 nm, dotted lines) and emission (λ_{ex} = 540 nm, solid lines) spectra of RB-MSNs 1% (curve a), RB-MSNs 4% (curve b) and RB-MSNs 10% (curve c). In the inset emission and excitation spectra of RB in water solution are reported for comparison.

Table 4 – The emission positions of RB-MSNs systems compared to RB in water solution and I_1/I_2 ratios.

Samples	λ_1 (nm)	λ_2 (nm)	I_1/I_2 (em)
RB in water solution	563	611	3.42
RB-MSNs 1%	583	620	1.92
RB-MSNs 4%	588	627	1.81
RB-MSN 10%	590	627	1.60

λ_1 is the maximum, λ_2 is the shoulder. I_1/I_2 is the ratio of the intensities of the main band and the shoulder in the emission spectra.

The variation of the RB triplet state energy level upon adsorption can be estimated by TD-DFT calculations as well, both for the isolated dianion molecule and for the RB-MSNs model cluster described above. The theoretical approach was the same as for the simulation of the absorption spectra (see above), and T1 energy was evaluated as the first TD-DFT root in the triplet spin state; in this case, as just one root has to be computed, the calculation could by performed on the whole RB-MSNs cluster. The computed T1 energies with respect to the ground state are +1.52 eV for isolated RB and +1.34 eV for the adduct, with a marked reduction after addition. Both states, at this theory level, are mainly due to HOMO-LUMO transitions: however, as shown in Figure S6 in the Supplementary Information, the HOMO electron density is quite different in the two cases, being concentrated on the carboxylate group in isolated RB, and on the xanthene moiety in the adduct. On the other hand, the LUMO density is quite similar in the two cases. The HOMO density difference is easily explained by the negative charge existing in the carboxylate group, and absent after the addition to the MSNs amine residue.

3.3 Evaluation of $^1O_2$ delivery.

The release of $^1O_2$ was evaluated by a chemical method using uric acid (UA), which undergoes oxidation during PS illumination. UA is an excellent singlet oxygen captor and it has been used in indirect quantitative determination of the photodynamic activity of many compounds.[27,28] Once the PS is excited, it undergoes an intersystem conversion process to the triplet state, which transfers energy to molecular oxygen in the solution to form $^1O_2$ that will further react with the uric acid. The absorption band of uric acid (292 nm) is not overlapped with the RB absorption band and it is not affected by the light exposure. The experiments were carried out in buffer pH 7.0 solution irradiated at 540 nm both for RB in water solution and RB-MSNs solid nanoparticles and the band decay due to the UA oxidation was monitored by UV-Vis spectroscopy for 80 min. A direct comparison of the $^1O_2$ delivery efficiency between RB in solution and RB attached to MSNs cannot be done directly because the analyses using nanoparticles demand their suspension, which affects the spectroscopic response due to the light scattering. Thus, to account the effects related to the insertion of RB into the MSNs, the evaluation of the $^1O_2$ delivery efficiency ($\eta_{RB\text{-}MSNs}$), using equation 1, was applied. The decomposition kinetics of the UA, monitored at 292 nm in the presence of free RB, was fitted to the first order kinetic model with two consecutives steps.[26] The decreasing of the UA absorption as a function of illumination time of the free RB and RB-MSNs nanoparticles are reported in Figure S5 of the Supporting Information. In the case of RB in water solution (Fig. S7A), besides the decreasing of the band at 292 nm, a shift to 315 has also been observed, being attributed to a complex reaction. For this reason, the time selected, as the standard value of RB for the equation 1 was the one associated with the slowest kinetic reaction (t_{RB}=31.4 min). In the case of RB-MSNs solid materials (Fig. S7 B,C and D in the Supporting Information) the formation of intermediate products is not visible due to the scattering of light by the nanoparticles that produce very broad absorption bands. In this sense, the UA decay kinetics related to the RB-MSNs systems could be better fitted using a first order exponential decay model.

Firstly, to be sure the UA band decreasing was induced by the formation of singlet oxygen in the solution, a control experiment has been carried out using plain NH_2-MSNs (Figure 9) whereby it is evident that irradiation at 540 nm during 80 min does not cause any alteration in the UA band in the absence of RB. The results related to the $^1O_2$ delivery efficiency ($\eta_{(RB\text{-}MSNs)}$) for the MSNs with different RB loadings are reported in Table 5, using the standard singlet oxygen yield for RB in water solution (Φ^1O_2= 0.75)[6] together with the values of time; the decay curves of the UA band are reported in Figure 9. The obtained values for RB-MSN 1% and 10% ($\eta_{RB\text{-}MSNs}$ = 0.31 e 0.15, respectively) are lower than the value calculated for RB-MSN 4% ($\eta_{RB\text{-}MSNs}$ = 0.74). This value is very close to the singlet oxygen quantum yield for RB in water solution, which means that this system has the optimal RB loading to produce efficiently $^1O_2$ and that the $^1O_2$ produced can oxidize the UA.

Table 5 – Efficiency of singlet oxygen delivery of RB-MSNs nanoparticles.

Samples	t (min)	R^2	$\eta_{RB\text{-}MSNs}$
RB-MSNs 1%	77.59	0.9912	0.31
RB-MSNs 4%	31.91	0.9992	0.74
RB-MSNs 10%	149.68	0.9879	0.15

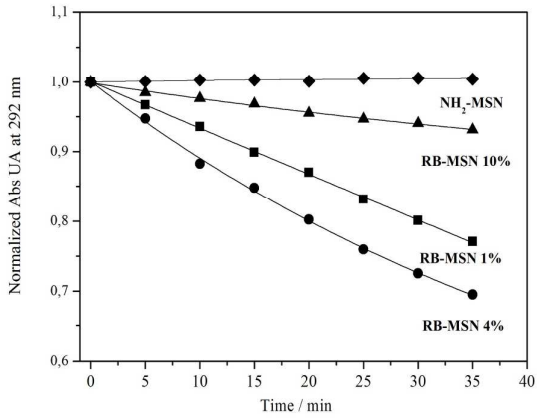

Fig. 9 – Decay curves of the UA absorption band at 292 nm as a function of the irradiation time in the presence of RB-MSNs and NH_2-MSNs.

The poor singlet oxygen efficiency of RB-MSN 1% and RB-MSNs 10% is related to the RB loading, in fact in the low loading sample, the amount of RB is not enough to deliver high concentration of singlet oxygen, while if the RB loading is too high (10%) the aggregate formation, that was evidenced by the spectroscopic studies, decreases the triplet state lifetime affecting the singlet oxygen efficiency.

The RB-MSNs nanoparticles with the optimum RB loading (4%) were tested in vitro using melanoma cells (SK-MEL-28).[23] In the presence of RB-MSNs 4%, the cell proliferation was reduced after light activation. The preliminary results were very promising and underlined the potential application of optimized RB-MSNs as a PDT device.

Conclusions

The presented study has evidenced that the covalent coupling of Rose Bengal photosensitizer into mesoporous silica nanoparticles offers a real advantage for PDT applications given that the PS molecules are stably incorporated into the nanoparticles and are protected from the outer environment. The loading of PS is a very important factor that affects the efficiency of singlet oxygen delivery. The detailed spectroscopic characterization performed by means of DR UV-

Vis and photoluminescence, combined with theoretical calculations, has evidenced that the PS loading has to be optimized in order to avoid the formation of aggregates that affect negatively the single oxygen generation. The optimized device with a 4% loading of Rose Bengal has shown promising performance in reducing cell proliferation upon illumination.[23]

Acknowledgements

The authors thank the Cariplo (Bando "Materiali Avanzati" 2011) and Prin2012 projects (MIUR Ministry of Education, University and Research) for financial support. B.M.E. thanks CAPES (Coordenação de Aperfeiçoamento de Pessoal de Nível Superior) for financial support.

References

1 V. Biju, *Chem. Soc. Rev.,* 2014, **43**, 744-764.
2 V. Mamaeva, C. Sahlgren and M. Lindén, M. *Advanced Drug Delivery Reviews,* 2013, **65**, 689–702.
3 W.X. Mai and H. Meng, *Integr. Biol.,* 2013, **5**, 19-28.
4 H.S. Peng and D.T. Chiu, *Chem. Soc. Rev.,* 2015**,** DOI: 10.1039/C4CS00294F.
5 a) G. R. Fleming, A.W.E. Knight, J.M. Morris, B.J.S. Morrison and G.W. Robinson, *J. Am. Chem. Soc*., 1977, **99**, 4306-4311. b) D.C. Neckers, *J. Photochem. Photobiol. A: Chemistry,* 1989, **47**, 1-29.
6 E. Gandin, Y. Lion and A. Van der Vorst, *Photochem. Photobiol*., 1983, **37**, 271-278.
7 R.W. Redmond and J.N. Gamlin, *Photochem. Photobiol*., 1999, **70**, 391-475.
8 T. Zhao, X. Shen, L. Li, Z. Guan, N. Gao and P. Yuan, *Nanoscale* 2012, **4**, 7712-7719.
9 J. Lenard, A. Rabson and R. Vanderoef, *Proc. Natl. Acad. Sci*., 1993, **90**, 158-162.
10 S.K. Srivastava and M.J. Modak, *Biochemistry (Mosc.),* 1983, **22**, 2283-2288.
11 M. Schafer, C. Schmitz, R. Facius, G. Horneck, B. Milow, K.-H Funnken and J. Ortner, *Photochem. Photobiol*. 2000, **71**, 514-523.
12 J. Cui, J. Jin, Y.-H. Hsieh, H. Yang, B. Ke, K. Damera, P.C. Tai and B. Wang, *ChemMedChem,* 2013, **8**, 1384 – 1393
13 J.P. Celli, B.Q. Spring, I. Rizvi, C.L. Evans, K.S. Samkoe, S. Verma, B.W. Pogue and T. Hasan, *Chem. Rev.,* 2010, **110**, 2795–2838.
14 B.W. Henderson and T.J. Dougherty, *Photochemistry and Photobiology*, 1992, **55**, 145–157.
15 C.A. Robertson, D. Hawkins Evans and H. Abrahams, *J. Photochem. Photobiol. B: Biology*, 2009, **96**, 1–8.
16 M.C. DeRosa and R.J. Crutchley, *Coordination Chemistry Reviews,* 2002, **233-234**, 351-371.
17 J. Jori, *J. Photochem. Photobiol. B: Biology,* 1996, **36**, 89-106
18 E. Fischer and F. Varga, *Acta Physiol. Acad. Sci. Hung*., 1979, **54**, 89-94.
19 C.-K. Lim, J. Heo, S. Shin, K. Jeong, Y.H. Seo, W.-D. Jang, C.R. Park, S.Y. Park, S. Kima and I.C. Kwon, *Cancer Lett*., 2012, **334**, 176-187.
20 J.F. Lovell, T.W.B. Liu, J. Chen, and G. Zheng, *Chem. Rev*. 2010, **110**, 2839-2857.
21 T.L. Doane and C. Burda, *Chem Soc Rev*, 2012, **41**, 2885-2911.
22 L. Cheng, C. Wang, L. Feng, K. Yang and Z. Liu, *Chem. Rev.*, 2014, **114 (21)**, 10869–10939.
23 E. Gianotti, B. Martins Estevao, F. Cucinotta, N. Hioka, M. Rizzi, F. Renò, and L. Marchese, *Chem. Eur. J.,* 2014, **20**, 10921-10925.
24 D.R. Radu, C.-Y. Lai, K. Jeftinija, E.W. Rowe, S. Jeftinija and V.S.-Y. Lin, *J. Amer. Chem. Soc.,* 2004, **126**, 13216-13217.
25 J. Landers, G. Gor and A.V. Neimark, *Colloids Surf. A*, 2013, **437**, 3-32.
26 B. Ribeiro Rabello, A. Passarella Gerola, D. Silva Pellosi, A. Luiz Tessaro, J. Leandro Aparicio, W. Caetano and N. Hioka, *J. Photochem. Photobiol. A: Chemistry,* 2012, **238**, 53-62.
27 A. Passarella Gerola, J. Semensato, D. Silva Pellosi, V. Roberto Batistela, B. Ribeiro Rabello, N. Hioka and W. Caetano, *J. Photochem. Photobiol. A: Chemistry,* 2012, **232**, 14-21.
28 a)L.M. Rossi, P.R. Silva, L.L.R. Vono, A.U. Fernandes, D.B. Tada and M.S. Baptista, *Langmuir,* 2008, **24**, 12534-12538. b) P.R. Silva, L.L.R. Vono, B.P. Esposito, M.S. Baptista and L.M. Rossi, *Phys.Chem.Chem.Phys*., 2011, **13**, 14946-14952.
29 A.D. Becke, *J. Chem. Phys.,* 1993, **98**, 5648-5652.
30 P.C. Hariharan and J.A. Pople, *Theor. Chim. Acta,* 1973, **28**, 213-222.
31 T.H. Dunning, *J. Chem. Phys.,* 1989, **90**, 1007-1023.
32 P.J. Hay and W.R. Wadt, *J. Chem. Phys.,* 1985, **82**, 270-283.
33 W.R. Wadt and P.J. Hay, *J. Chem. Phys.,* 1985, **82**, 284-298.
34 P.J. Hay and W.R. Wadt, *J. Chem. Phys.,* 1985, **82**, 299-310.
35 M. Cossi, N. Rega, G. Scalmani and V. Barone, *J. Comput. Chem.,* 2003, **24**, 669-681.
36 J.P. Perdew, K. Burke and M. Ernzerhof, *Phys. Rev. Lett*., 1996, **77**, 3865-3868.
37 K.J. Edler, P.A. Reynolds, J.W. White and D. Cookson, *J. Chem. Soc. Faraday Trans.,* 1997, **93**, 199-202.
38 C.T. Kresge, M.E. Leonowicz, W.J. Roth and J.C. Vartuli, *Nature,* 1992, **359**, 710-712.
39 D. W. Sindorf, and G. E. Maciel, *J. Am. Chem. Soc*., 1983, **105**, 3767-3776.
40 J. J. Yang, I. M. El-Nahhal, I-S. Chuang and G. E. Maciel, *J. Non-Cryst. Solids,1997,* **209**, 19–39.
41 K. Liu, X. Liu, Q. Zeng, Y. Zhang, L. Tu, T. Liu, X. Kong, Y. Wang, F. Cao, S.A.G. Lambrechts, SM.C.G. Aalders and H. Zhang, *ACS Nano*, 2012, **6**, 4054-4062.
42. P. Ugliengo, M. Sodupe, F. Musso, I.J. Bush, R. Orlando and R. Dovesi, *Adv. Mater.,* 2008*,* **20**, 4579–4583.
43. D. Xu and D.C. Neckers, *J. Photochem. Photobiol. A: Chemistry*, 1987, **40**, 361-370.
44. M.E. Daraio and E. San Román, *Helvetica Chimica Acta*, 2001, **84**, 2601-2614;
45. H.B. Rodrìguez, M.G. Lagorio and E. San Román, *Photochem. Photobiol. Sci*., 2004, **3**, 674-680.
46. S.D.-M. Islam and O. Ito, *J. Photochem. Photobiol. A: Chemistry,* 1999, **123**, 53-59